



Electrodeposition of indium antimonide (InSb) from dimethyl sulfoxide-based electrolytes

Wouter Monnens¹ · Naomi Billiet² · Koen Binnemans² · Jan Fransaer¹

Received: 22 February 2024 / Revised: 22 May 2024 / Accepted: 23 May 2024 / Published online: 18 June 2024
© The Author(s), under exclusive licence to Springer-Verlag GmbH Germany, part of Springer Nature 2024

Abstract

Indium antimonide (InSb) is a III-V compound semiconductor with a narrow bandgap and a high electron mobility, and is used in various optoelectronic devices. Electrodeposition represents a low-cost, scalable method for fabricating InSb films. In the literature, aqueous electrolytes and ionic liquids have commonly been applied. In this work, the electrodeposition of InSb films and nanowires from a dimethyl sulfoxide (DMSO)-based electrolyte was demonstrated. This electrolyte enabled electrodeposition in a broader potential range and at higher temperatures as compared to aqueous electrolytes. The electrolyte has a lower viscosity than ionic liquids, therefore exhibiting better mass transport properties for electrodeposition. It was shown that antimony(III) chloride, a precursor that is commonly used for InSb electrodeposition, leads to the formation of the metastable “explosive” antimony allotrope. Instead, self-prepared antimony(III) nitrate and indium(III) methanesulfonate were used, and were proven to be suitable precursors. Electrolytes with a 5:1 indium-to-antimony precursor molar ratio enabled electrodeposition of InSb films at 21 °C and 120 °C on platinum and n-type InSb(400), as well as electrodeposition of InSb nanowires in anodized aluminum oxide templates. The morphology, elemental composition and crystallinity of as-deposited InSb was analyzed using scanning electron microscopy (SEM), energy-dispersive X-ray spectroscopy (EDX) and X-ray diffraction (XRD), respectively. It was demonstrated that the film quality did not improve at 120 °C. Tauc plots from FT-IR transmission measurements were used for the determination of the bandgap of the deposits. The bandgap of the InSb films on platinum was 0.159 eV at 21 °C and 0.168 eV at 120 °C, whereas the bandgap of the InSb film deposited at 120 °C on InSb(400) was 0.186 eV.

Introduction

III-V compound semiconductors have been intensively investigated over the last 50 years [1, 2]. Due to their unique properties, they find many applications and are incorporated in numerous electronic consumer products, as well as in advanced electronics and optoelectronics devices [3, 4]. One such binary III-V semiconductor is indium antimonide (InSb). This material exhibits a small band gap of 0.17 eV at 27 °C. Its hole mobility is 800 cm² V⁻¹s and its electron mobility is 78,000 cm² V⁻¹s at 27 °C, which are among the highest values of all semiconductors [5–7]. InSb has been

fabricated in the form of films, nanowires, nanoparticles and quantum wells, and is primarily utilized in optoelectronics devices such as wide-range infrared detectors and sensors [6, 8–13]. It is typically produced via vacuum techniques such as chemical vapor deposition, vapor phase epitaxy or molecular beam epitaxy [14–18]. These techniques have been proven to provide high-quality monocrystalline materials, yet, they require expensive equipment, toxic and volatile precursors and deposition rates are slow. To mitigate these disadvantages, various alternative, cheap (wet chemical) production methods such as electrodeposition have been explored [19]. Despite its inability to yield the ultra-flat monocrystalline materials fabricated by vacuum techniques, electrodeposition is a promising method for the production of a number of semiconductors and is particularly favorable due to its simplicity and flexibility, and its cost-effectiveness in terms of equipment and required chemicals [20–22].

InSb thin films and nanowires has been electrodeposited from a variety of aqueous electrolytes [23–32]. Although electrodeposition of InSb from aqueous solutions is

✉ Jan Fransaer
Jan.fransaer@kuleuven.be

¹ KU Leuven, Department of Materials Engineering, Kasteelpark Arenberg 44, P. O. box 2450, B-3001 Leuven, Belgium

² KU Leuven, Department of Chemistry, Celestijnenlaan 200F, P. O. box 2404, B-3001 Leuven, Belgium

possible, it contends with hydrogen evolution if applied current densities are high, leading to the formation of porous, non-compact, rough films, or to the formation of indium(III) oxide [31, 33–36]. Furthermore, in some cases, heat treatment is required after electrodeposition to improve crystallinity [37]. InSb electrodeposition has also been explored from a variety of non-aqueous baths such as molten salts and ionic liquids [38–40]. These media enable electrodeposition in a broad potential range and at elevated temperatures. This results in higher deposition rates and thermal annealing may not be necessary. However, electrochemically stable molten salts and ionic liquids are viscous at room temperature, and can be expensive. In a previous study, we investigated the electrochemical behavior and electrodeposition of indium at room temperature and above its melting point, at 160 °C, from an electrolyte composed of indium(III) methanesulfonate ($\text{In}(\text{CH}_3\text{SO}_3)_3$) and dimethyl sulfoxide (DMSO) [41]. DMSO is a widely used solvent. Its electrochemical window is wider and its boiling point (189 °C) is higher than that of water. Moreover, DMSO exhibits a lower viscosity and is less expensive than most electrochemically stable ionic liquids, and is therefore a more interesting alternative. Its electrochemical stability allows for electrodeposition at higher current densities, and its high boiling point allows for electrodeposition at temperatures above 100 °C. In this work, we modified the electrolyte used previously for indium electrodeposition by addition of a suitable antimony precursor and investigated the electrodeposition of crystalline InSb films at both room and elevated temperature. It was postulated and tested whether deposition at higher temperatures would improve the crystallinity of the film. Moreover, the electrodeposition of InSb nanowires was investigated using anodized aluminum oxide (AAO) substrates as templates.

Experimental

Products

Dimethyl sulfoxide (DMSO, anhydrous, 99.9%), silver nitrate (AgNO_3 , 99.8%), antimony(III) chloride (SbCl_3 , 99.0%), and tetraethylammonium perchlorate (TEAClO_4 , 99%) were purchased from Sigma-Aldrich (Overijse, Belgium). Indium(III) oxide (In_2O_3 , 99%) and potassium bromide (KBr , 99%) were purchased from Thermo Fisher (Merelbeke, Belgium). Methanesulfonic acid (MSA, 99.5%) was purchased from Carl Roth (Karlsruhe, Germany). Hydrochloric acid (HCl 37%, analytical grade) and sodium hydroxide (NaOH, analytical grade) were purchased from VWR (Oud-Heverlee, Belgium).

Instrumentation

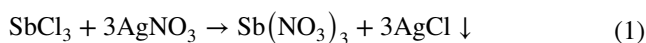
All electrochemical experiments were performed in an argon-filled glovebox with oxygen and moisture concentrations below 1 ppm. An Autolab PGSTAT 302 N potentiostat, controlled by a computer with NOVA2 software was used in combination with a three-electrode setup. For recording cyclic voltammograms (CVs), a circular platinum (Pt) disk electrode (4 mm diameter) embedded in glass served as the working electrode (WE). For electrodeposition experiments, platinum coated silica wafers with titanium buffer layers (25 nm Pt) and Si-coated n-type InSb wafers (25 nm InSb, donor conc. $5 \times 10^{16} \text{ cm}^{-3}$) with an approximate surface area of 25 mm^2 were used as substrates. For all experiments, the counter electrode (CE) consisted of a graphite rod whose area was at least five times larger than that of the WE. Prior to performing measurements, the electrodes were ultrasonicated in ethanol and air-dried. Platinum electrodes were ultrasonicated in ethanol; subsequently washed with hydrochloric acid (35%), rinsed with demineralized water and ethanol, and air-dried. The reference electrode (RE) was a silver/silver(I) ($\text{Ag}/\text{Ag}(\text{I})$)-based electrode consisting of a glass tube, filled with a solution of 0.01 M silver(I) nitrate (AgNO_3) and 0.1 M tetraethylammonium perchlorate (TEAClO_4) in DMSO, in which a silver wire with a diameter of 1 mm was immersed. The potential of this reference electrode for acetonitrile instead of DMO has been reported to be roughly +0.36 V vs. SHE. It is assumed that our reference electrode likely exhibits a similar potential.

For nanowire electrodeposition, AAO films on aluminum foil (bought from InRedox, USA) were used as substrates. These AAO films had a thickness of 2 μm , with a pore density of $1.5 \times 10^9 \text{ cm}^{-2}$. The average pore diameter was 120 nm. Pieces were cut and mounted in a sample holder (bought from Redoxme AB, Sweden) with a nominal aperture of 1 cm^2 . Prior to use, the substrates were immersed in a 5 wt% phosphoric acid solution to etch away the barrier layer of the aluminum base. The substrate was washed with ethanol and subsequently air-dried. After nanowire deposition, the AAO template was either partly or fully etched away by immersion in a 0.5 M of NaOH. A glass beaker was used as the electrochemical cell to which 10 mL of solution was added. CVs were always started at the open circuit potential (OCP) and scanned first towards cathodic overpotentials. All CVs in this work are the first recorded cycle. The structural morphology of the prepared deposits was studied by scanning electron microscopy (SEM) on a FEI Nova 600 Nanolab NanoSEM. Energy-dispersive X-ray spectroscopy (EDX) with an octane elite super silicon drift detector (Ametek

EDAX) was used for elemental analysis. For all measurements, the acceleration voltage was 10 keV. X-ray diffraction (XRD) was measured using a Bruker D2 Phaser X-ray diffractometer. For FT-IR measurements, samples were prepared by carefully scraping off InSb films that were electrodeposited on wafer substrates. 200 mg of InSb and 1.8 g of dried KBr were subsequently mixed and grounded using an agate pestle and mortar. Pellets were then pressed with a Specac 13 mm pellet die and a Specac hydraulic pellet press. 8 tons of pressure was applied, while applying vacuum (1–3 mbar) using a Pascal 2015SD vacuum pump. FT-IR spectra were measured in transmission mode on a Bruker Vertex 70 FT-IR spectrometer from 4000 cm^{-1} to 400 cm^{-1} at a resolution of 4 cm^{-1} .

Synthesis

$\text{Sb}(\text{NO}_3)_3$ was synthesized by mixing 0.1 M of SbCl_3 and 0.3 M of AgNO_3 in a molar ratio of 1:3 in 10 ml of DMSO (1). A small excess of AgNO_3 was added to avoid the presence of chlorides in the final solution.



The mixture was filtered to remove the precipitated AgCl . The small amount of silver ions left in the solution was removed by electrolysis, by applying -0.45 V vs. Ag^+/Ag for 24 h on a cylindrical platinum-coated mesh electrode. Here, the CE and RE were a graphite rod and the Ag^+/Ag -based electrode, respectively. The solution was stirred at 700 rpm. After electrolysis, a thin layer of silver metal was observed on the mesh electrode. The final solution was transparent and colorless. $\text{In}(\text{CH}_3\text{SO}_3)_3$ was synthesized following a procedure described in our previous work [41].

Results and discussion

Cyclic voltammetry of individual precursors

To achieve electrodeposition of stoichiometric InSb, understanding of the electrochemical window of the solvent and the overpotentials at which electrodeposition of the individual components takes place is necessary. Therefore, cyclic voltammograms (CVs) were recorded for electrolytes composed of (Fig. 1a) 0.1 M of TEAClO_4 in DMSO, (Fig. 1b) 0.1 M of $\text{In}(\text{CH}_3\text{SO}_3)_3$ in DMSO, (Fig. 1c) 0.1 M of SbCl_3 in DMSO, and (Fig. 1d) 0.1 M of $\text{Sb}(\text{NO}_3)_3$ in DMSO. Both commercial SbCl_3 and self-prepared $\text{Sb}(\text{NO}_3)_3$ were selected as potential antimony precursors as they exhibited sufficient solubilities (>0.1 M) in DMSO. The CV in Fig. 1a shows the electrochemical window of DMSO. TEAClO_4 was used here as inert background salt. The blue lines mark the

cathodic and anodic limits yielding a window of 4 V. CV in Fig. 1b shows the electrochemical behavior of $\text{In}(\text{CH}_3\text{SO}_3)_3$ in DMSO. The observed features and the corresponding electrochemical processes have been thoroughly discussed in a previous work [41]. In summary, in the cathodic wave, indium(III) is reduced to both indium(I) and indium metal. Yet, reduction to metallic indium was found to be the predominant process, corresponding to 94% of the cathodic current efficiency. The remaining 6% is likely due to formation of indium(I) species. This unstable species reacts away via a disproportionation reaction ($3\text{In}(\text{I}) \rightarrow \text{In}(\text{III}) + 2\text{In}(\text{0})$). During stripping, indium metal is oxidized to indium(I).

The CV in Fig. 1c and d show the electrochemical behavior of SbCl_3 and $\text{Sb}(\text{NO}_3)_3$ in DMSO, respectively. For both CVs, the onset in reduction current in the forward scan initiates at -0.55 V vs. Ag^+/Ag (indicated by the green lines). Notably, the reduction current for the $\text{Sb}(\text{NO}_3)_3$ -containing electrolyte increases much more abruptly. Moreover, it forms a nucleation loop in the backward scan, which is indicative of metal(loid) electrodeposition. This is not the case for the CV recorded for the SbCl_3 -containing electrolyte. Although it is assumed that the processes in both CVs involve the reduction of antimony(III) to antimony metal, the difference in the cathodic current trends in the two CVs indicates a disparity in antimony electrodeposition. Multiple studies demonstrate that the electrodeposition of antimony from chloride-containing electrolytes can lead to the formation of an amorphous allotrope, “*explosive antimony*”, which contains significant amounts of halogen impurities [42–45]. A possible explanation for the observed difference in cathodic behavior between both CVs might therefore be the formation of this amorphous allotrope from the chloride-containing electrolyte, as opposed to the formation of pure antimony from the nitrate-containing electrolyte. Furthermore, the CVs both show oxidation peaks in the backward scan, initiating at -0.50 V vs. Ag^+/Ag and -0.33 V vs. Ag^+/Ag , respectively. These are ascribed to the stripping of the as-deposited antimony to antimony(III) species. The accumulated charge during the cathodic waves is larger than that of the stripping peaks, indicating that antimony electrodeposition is not fully reversible. Possibly, antimony nuclei formed (an) alloy(s) with the platinum substrate, which were not stripped in the investigated potential region [46].

Electrodeposition of indium and antimony

Subsequently, it was investigated whether pure antimony could be electrodeposited from the electrolytes composed of 0.1 M of SbCl_3 in DMSO, and 0.1 M of $\text{Sb}(\text{NO}_3)_3$ in DMSO, respectively, by applying -1.0 V vs. Ag^+/Ag on a platinum substrate at 21 °C. Indium was electrodeposited from 0.1 M of $\text{In}(\text{CH}_3\text{SO}_3)_3$ in DMSO by applying -1.6 V vs. Ag^+/Ag on a platinum substrate at 21 °C. The resulting

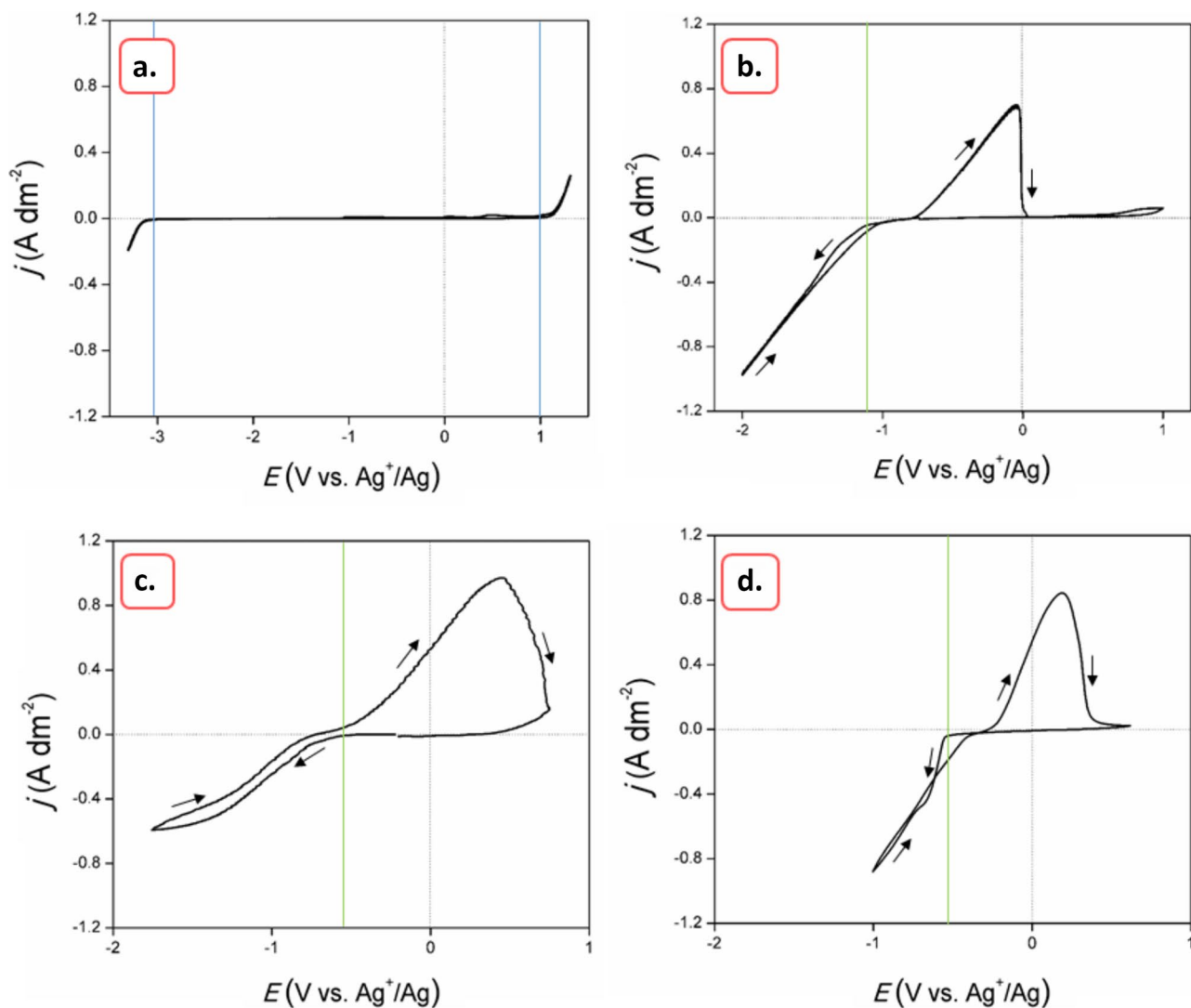
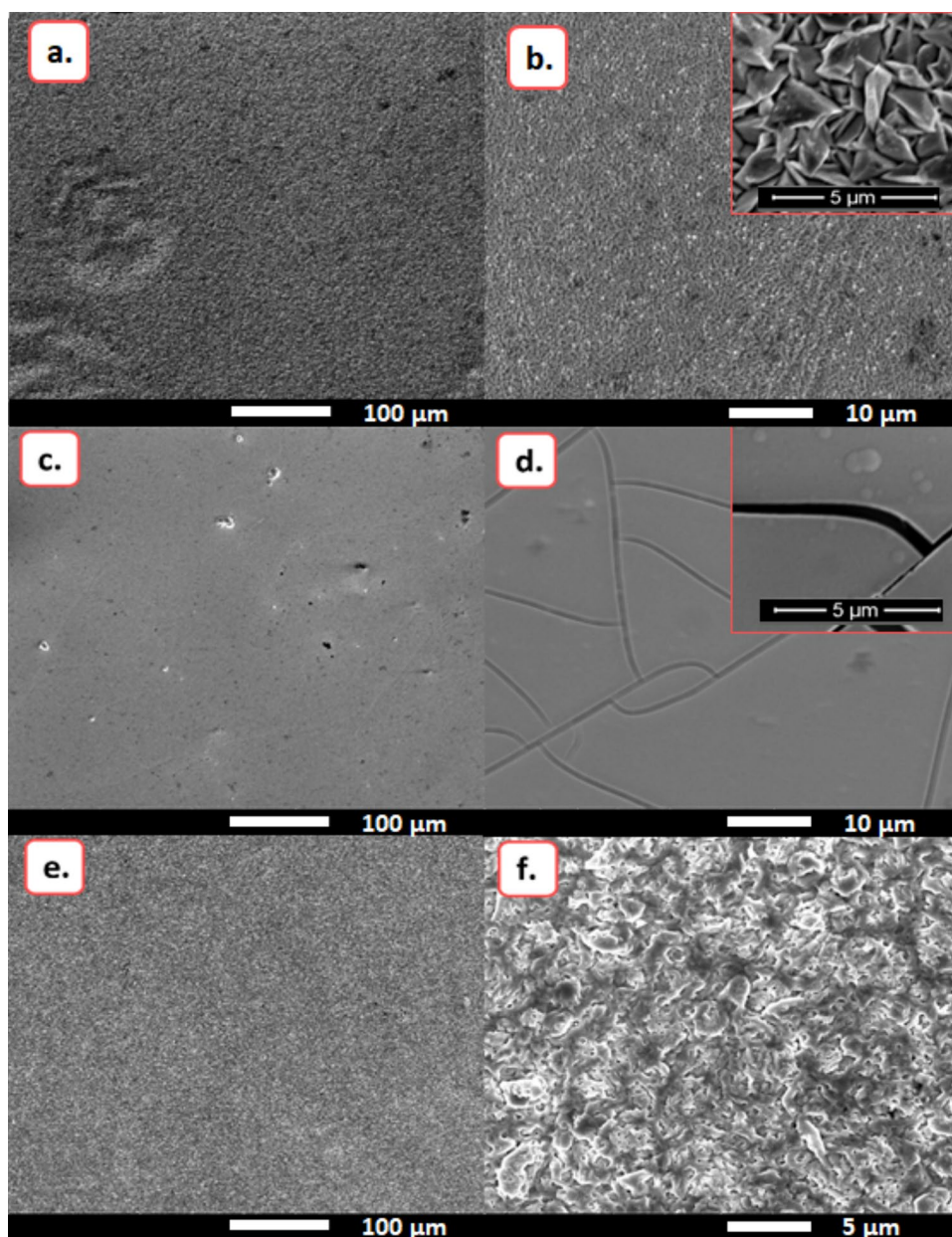


Fig. 1 **a** CV of 0.1 M of TEAClO₄ in DMSO, **b** CV of 0.1 M of In(CH₃SO₃)₃ in DMSO, **c** CV of 0.1 M of SbCl₃ in DMSO, and **d** CV of 0.1 M of Sb(NO₃)₃ in DMSO, recorded on a circular platinum WE, at a scan rate of 20 mV s⁻¹, at 21 °C

antimony and indium deposits were analyzed using scanning electron microscopy (SEM). Figure 2a and b show the SEM images of electrodeposited antimony from the Sb(NO₃)₃-based electrolyte. The deposited film consists of triangular-shaped microstructures that overlap with each other. This morphology has been reported before for electrodeposited antimony from both aqueous and non-aqueous electrolytes [47–49]. Figure 2c and d show the SEM images of electrodeposited antimony from the SbCl₃-based electrolyte. The images show that the morphology of the deposit is a cracked layer with nearly no features. Only a few spheres can be seen from the highest magnification SEM image insert in Fig. 2b. It is suspected that the deposited layer is the “*explosive antimony*” allotrope, formed by incorporation of chlorides that are present in the electrolyte. Wu et al. reported the electrodeposition of explosive antimony from

an electrolyte composed of SbCl₃ in ethylene glycol, and demonstrated that the deposits were amorphous and had featherlike flat structures, not completely dissimilar to the structures seen here [43]. Figure 2d and e show the SEM images of electrodeposited indium. The film is composed of soft interwoven structures. This film morphology is typical for electrodeposited indium, and has been reported in various others works [50–52]. Energy-dispersive X-ray spectroscopy (EDX) spectra of the three deposits are shown in Fig. 3. The EDX spectrum of the deposit obtained from the Sb(NO₃)₃-based electrolyte is shown in Fig. 3a, and reveals that this layer is composed purely of antimony. The EDX spectrum of the deposit obtained from the SbCl₃-containing electrolyte is shown in Fig. 3b, and shows that the deposit contains chlorine impurities. Upon scratching the deposited layer, white fumes were observed, indicating that amorphous

Fig. 2 **a, b** SEM images of crystalline antimony, electrodeposited from 0.1 M of $\text{Sb}(\text{NO}_3)_3$ in DMSO. **c, d**, SEM images of “*explosive antimony*”, electrodeposited from 0.1 M of SbCl_3 in DMSO. **e-f**, SEM images of indium, electrodeposited from 0.1 M of $\text{In}(\text{CH}_3\text{SO}_3)_3$ in DMSO. All films were electrodeposited on platinum substrates at 21 °C. Both antimony deposits were made at -1.0 V vs. Ag^+/Ag , while the indium was deposited at -1.6 V vs. Ag^+/Ag . The applied SEM acceleration voltage equaled 10 keV



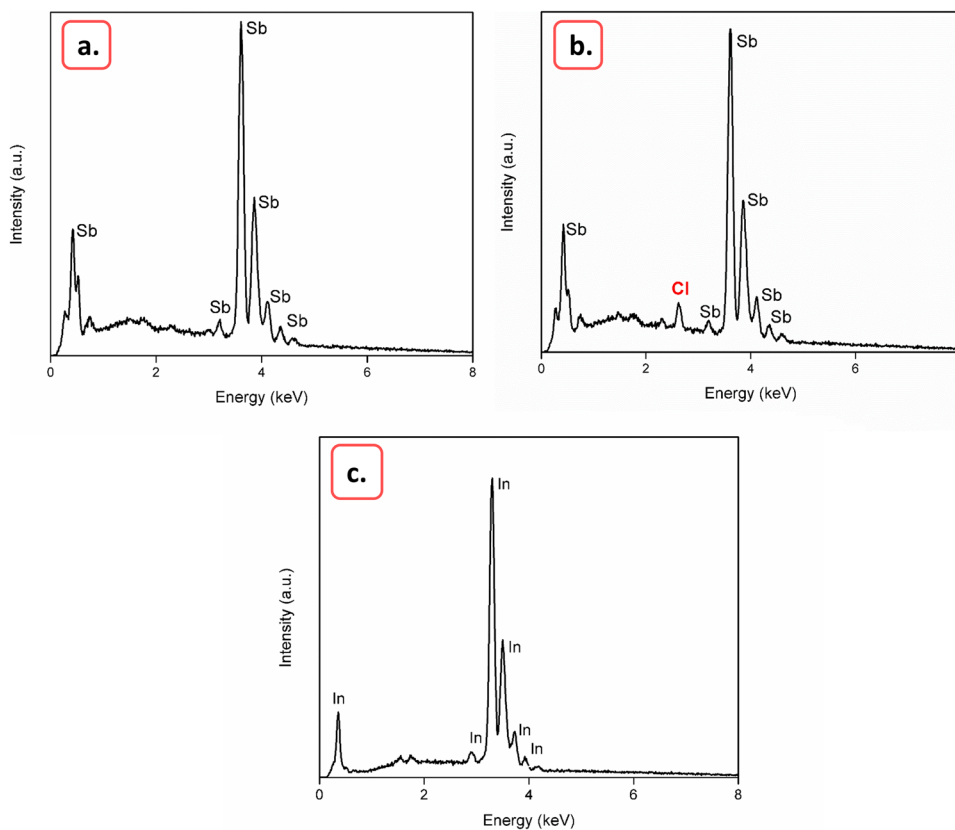
“*explosive antimony*” is indeed formed. Undoubtedly, the formation of this metastable phase is undesirable for the electrodeposition of InSb. The EDX spectrum of the indium deposit is shown in Fig. 3c, and shows that it is without impurities. This is in good agreement with the results from our previous study.

Cyclic voltammetry of the mixed electrolyte

Since $\text{In}(\text{CH}_3\text{SO}_3)_3$ and $\text{Sb}(\text{NO}_3)_3$ enable pure indium and antimony deposits, they are appropriate precursors for InSb electrodeposition. Consequently, a mixed electrolyte was prepared composed of 0.1 M of $\text{In}(\text{CH}_3\text{SO}_3)_3$ and 0.02 M of $\text{Sb}(\text{NO}_3)_3$ in DMSO, and investigated for the

electrodeposition of InSb. The molar ratio of indium to antimony was kept at 5:1 since the CVs of the individual components indicate that indium(III) reduction occurs at significantly more negative potentials than antimony(III) reduction ($\Delta V_{\text{onset}} \approx 600$ mV). CVs were recorded for this mixed electrolyte at 21 °C (Fig. 4a) as well as at 120 °C (Fig. 4b). In the CV recorded at 21 °C, in the forward scan, three features can be observed; reduction peak *R1* located at -0.82 V vs Ag^+/Ag , cathodic wave *R2*, starting at -1.00 V vs. Ag^+/Ag , and cathodic wave *R2'* starting at -1.33 V vs. Ag^+/Ag , at which the cathodic current significantly increases. From the CVs recorded for the individual components, *R1* and *R2* can be ascribed to the reduction of antimony(III) to antimony and indium(III) to

Fig. 3 **a** EDX spectrum of antimony, electrodeposited from 0.1 M of $\text{Sb}(\text{NO}_3)_3$ in DMSO, **b** EDX spectrum of “explosive antimony”, electrodeposited from 0.1 M of SbCl_3 in DMSO, and **c** EDX spectrum of indium, electrodeposited from 0.1 M of $\text{In}(\text{CH}_3\text{SO}_3)_3$ in DMSO. All electrodeposits were made on platinum substrates at 21 °C. Both antimony deposits were made at -1.0 V vs. Ag^+/Ag , while the indium was deposited at -1.6 V vs. Ag^+/Ag . The applied SEM acceleration voltage equaled 10 keV



indium metal, respectively. The cathodic current increase observed at $R2'$ might be a consequence of electrodeposition of spontaneously formed InSb ($\Delta G_f^\circ \text{InSb} = -25.5 \text{ kJ mol}^{-1}$), occurring at increased rates over individual indium and antimony electrodeposition. However, this cannot be

stated with full certainty. In the backward scan, the oxidation peaks, $O1$ and $O2$, located at -0.85 V vs. Ag^+/Ag and 0.08 V vs. Ag^+/Ag , can be ascribed to the stripping of antimony and indium, respectively. Interestingly, $O1$ and $O2$ are notably smaller than the stripping peaks of

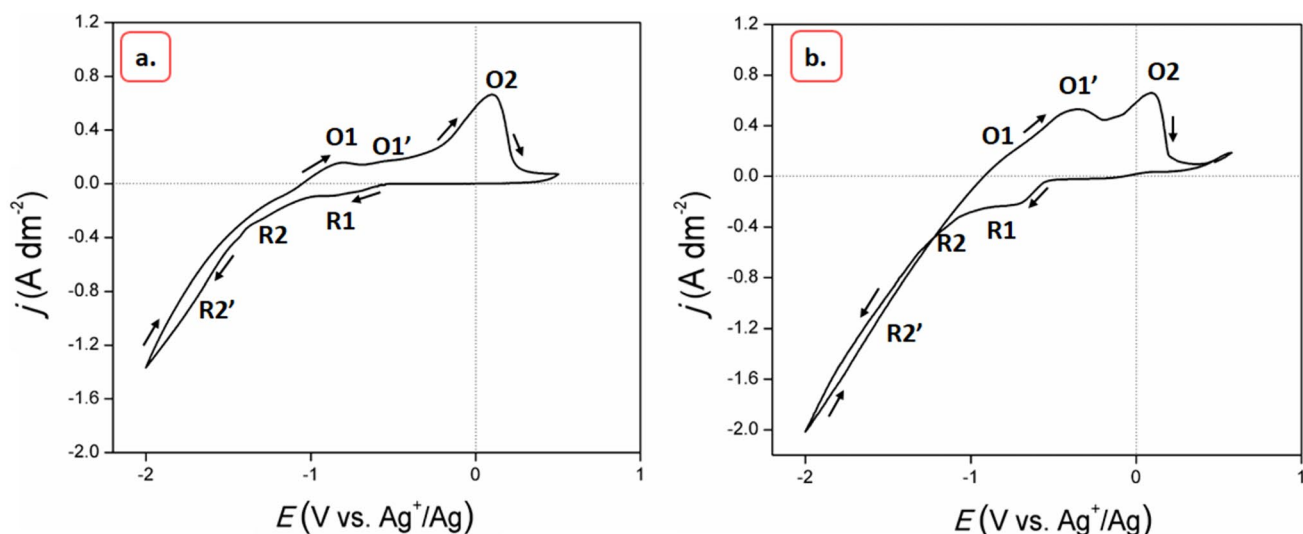
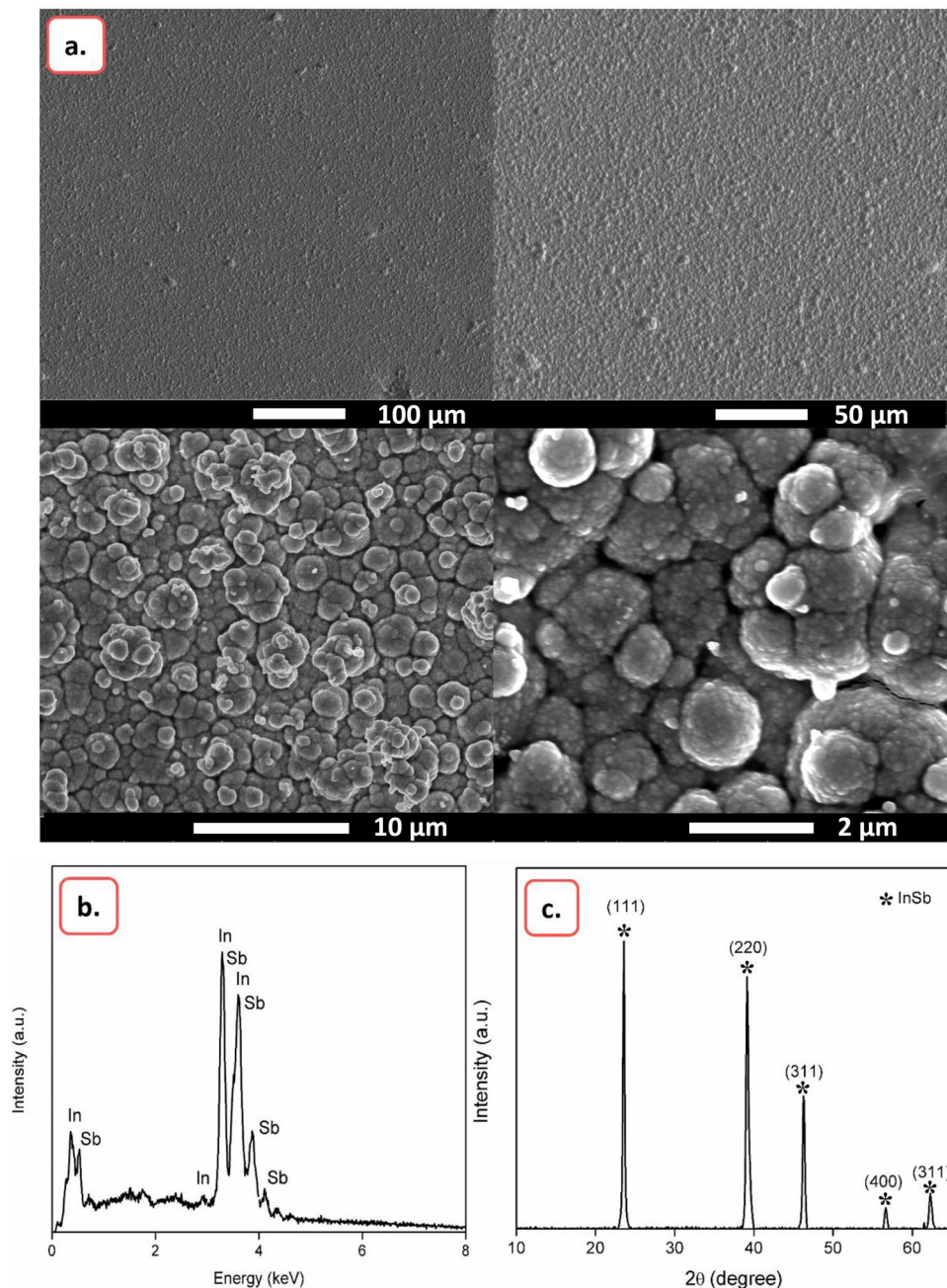


Fig. 4 CVs of 0.1 M $\text{In}(\text{CH}_3\text{SO}_3)_3$ and 0.02 M $\text{Sb}(\text{NO}_3)_3$ in DMSO, recorded on a circular platinum WE at 21 °C **a** and 120 °C **b**, at a scan rate of 20 mV s^{-1}

indium and antimony in the CVs shown in Fig. 1b and d. The subtle shoulder-like oxidation feature $O1'$, observed between $O1$ and $O2$, might be ascribed to stripping of formed InSb. Its formation could explain why $O1$ and $O2$ are smaller than the observed stripping peaks in the CVs of the individual components. In CV recorded at 120 °C, in the forward scan, analogous behavior is observed to that of CV (a). Features $R1$ at -0.75 V vs Ag^+/Ag , and $R2$, starting at -1.00 V vs Ag^+/Ag are once more ascribed to the reduction of antimony(III) to antimony and indium(III)

to indium, respectively, whereas $R2'$ could be due to electrodeposition of InSb. Observed current densities are higher compared to those in the CV recorded at 21 °C. This is due to increased kinetics of the electrochemical reactions and the lower viscosity of the electrolyte at 120 °C, which improves mass transport of the electroactive species towards the electrode. In the backward scan, $O1$ occurs as a subtle shoulder-like feature, followed by oxidation peak $O1'$, at -0.35 V vs. Ag^+/Ag . $O2$ is observed at 0.08 V vs. Ag^+/Ag . Clearly, $O1'$ is much larger here

Fig. 5 **a** SEM images at various magnifications, **b** EDX spectrum, and **c** XRD diffractogram of InSb electrodeposited at -1.6 V vs. Ag^+/Ag for 1 h on a platinum substrate at RT from an electrolyte composed of 0.1 M of $\text{In}(\text{CH}_3\text{SO}_3)_3$ and 0.02 M of $\text{Sb}(\text{NO}_3)_3$ in DMSO. The applied acceleration voltage for EDX and SEM was 10 keV



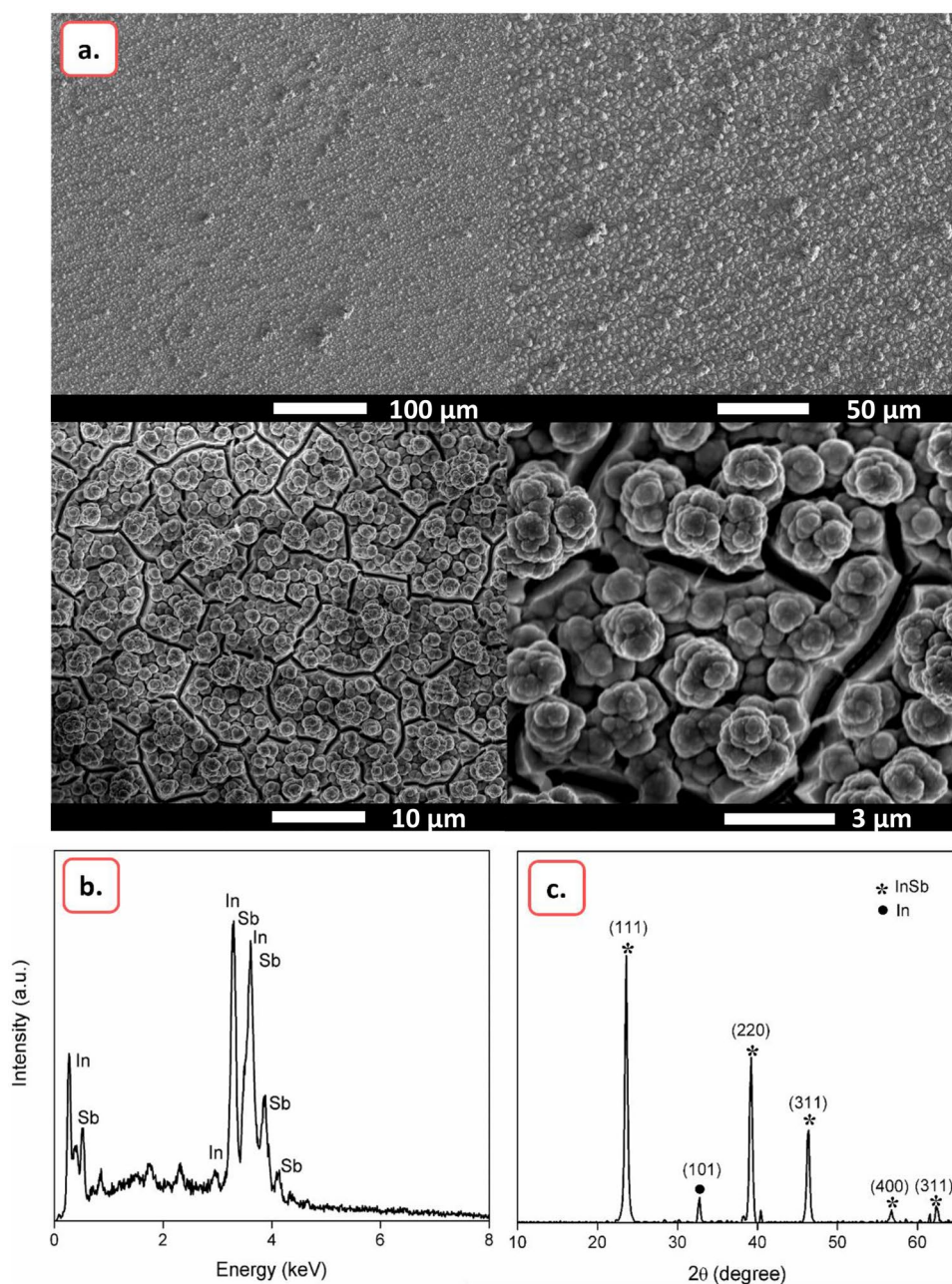
than in CV (a). This might be due to the more prominent formation of InSb at 120 °C; during the cathodic wave, a larger amount of indium and antimony nuclei are formed, grow, make contact, and spontaneously alloy, or InSb nuclei are directly formed [53, 54]. Consequently, in the backward scan, the InSb that formed is stripped, leading to a bigger stripping peak. The observation of this InSb stripping feature has also been reported by Yang et al. [38]. Yet, it is important to point out that just from the recorded CVs, it can only be speculated what the nature of the additional anodic and features is. Further analysis

is required to confirm the assignment to specific electrochemical reactions.

Electrodeposition of InSb films

First, electrodeposition of InSb at 21 °C was investigated. A potential of -1.6 V vs. Ag^+/Ag was applied for 1 h. on a platinum substrate using an electrolyte composed of 0.1 M of $\text{In}(\text{CH}_3\text{SO}_3)_3$ and 0.02 M of $\text{Sb}(\text{NO}_3)_3$ in DMSO. A stirring bar was added and rotated at 400 rpm to enhance mass transport. The attained deposit was analyzed using

Fig. 6 **a** SEM images at various magnifications, **b** EDX spectrum, and **c** XRD diffractogram of as-deposited InSb generated by applying -1.6 V vs. Ag^+/Ag for 1 h. on a platinum substrate at 120 °C from an electrolyte composed of 0.1 M of $\text{In}(\text{CH}_3\text{SO}_3)_3$ and 0.02 M of $\text{Sb}(\text{NO}_3)_3$ in DMSO. The applied acceleration voltage for EDX and SEM was 10 keV



SEM, EDX and XRD (Fig. 5). SEM images (Fig. 5a) reveal that a smooth film is attained. From higher magnification images, it is evident that this film consists of spherical-like particles that are grown together forming cauliflower-like structures. The EDX spectrum (Fig. 5b) shows peaks for antimony and indium. EDX indicates an approximate In/Sb ratio of 51/49 atomic %. This is a good approximation of the true In/Sb ratio, as the ratio given by EDX for a commercial InSb substrate was 50/50 atomic %. The XRD diffractogram (Fig. 5c) shows peaks for various InSb phases, indicating that the film is polycrystalline. The sharp and narrow nature of the diffraction peaks implies good crystallinity.

As DMSO is thermally stable over a broad temperature range, InSb films were also electrodeposited at 120 °C. Analogously to room temperature deposition -1.6 V vs. Ag^+/Ag was applied for 1 h. on a platinum substrate, using 0.1 M of $\text{In}(\text{CH}_3\text{SO}_3)_3$ and 0.02 M of $\text{Sb}(\text{NO}_3)_3$ in DMSO. The InSb film was investigated using SEM, EDX and XRD (Fig. 6). SEM images (Fig. 6a) reveal that the morphology of the film is very similar to the morphology of the deposit attained at 21 °C, be it slightly rougher. Cross-section SEM images of both deposits are shown in Fig. S1 in the Electronic Supporting Information (ESI). Contrary to the deposits at 21 °C, cracks are observed. These cracks are most probably the result of tensile stress caused by the difference in thermal expansion between the substrate and the deposited material. Since the platinum layer is very thin, the substrate will expand by the thermal expansion of the thick silicon layer. The linear thermal expansion coefficient of crystalline InSb (α_{InSb}) is $5.4 \times 10^{-6} \text{ }^\circ\text{C}^{-1}$ whereas that of silicon (α_{Si}) is $2.6 \times 10^{-6} \text{ }^\circ\text{C}^{-1}$. The thermal strain (ε_{TH}) for the InSb film on the substrate can be calculated by [55]:

$$\varepsilon_{\text{TH}} = (\alpha_{\text{InSb}} - \alpha_{\text{Si}})(T_d - T_m) \quad (2)$$

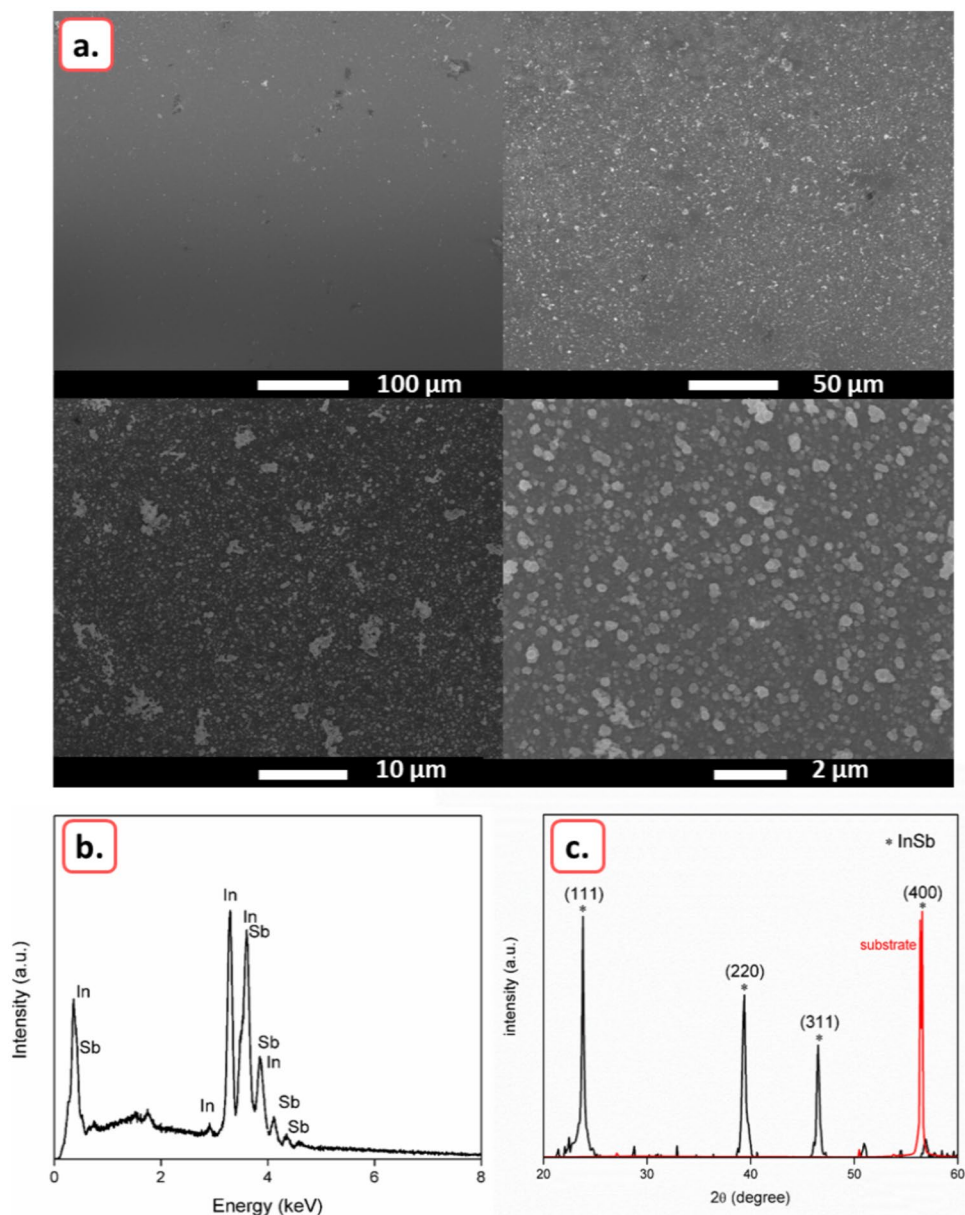
with T_d the temperature during deposition (120 °C) and T_m the temperature after cooling down (21 °C). ε_{TH} is found to be 2.74×10^{-4} . The positive value indeed indicates a tensile stress state. Stress can also be due to electrodeposition of the material itself (as growth stress), and due to the lattice mismatch between InSb (sphalerite crystal structure) and platinum (face-centered cubic crystal structure). When InSb is prepared via vacuum deposition techniques, a buffer layer is typically incorporated with a low lattice mismatch, resulting in strain relief and crack-free deposits. These buffer layers comprise of materials with sphalerite crystal structures, and are typically semiconductors with varying bandgap, or electrical insulators [56]. When using electrodeposition, such materials are either unusable or bring along additional challenges. As a consequence, the vast majority of studies reporting on the electrodeposition of InSb use metals or metal alloys as substrates. Several of them have also

reported cracks in the as-deposited InSb films and ascribed their occurrence to the large lattice mismatches [34]. The EDX spectrum (Fig. 6b) shows only peaks for antimony and indium. Quantitative analysis indicates an approximate In/Sb ratio of 51/49 atomic %. The diffractogram (Fig. 6c) shows a small peak for indium metal and sharp peaks for InSb at similar angles to those of the InSb deposited at 21 °C. However, due to the tensile stress in the layer, all peaks are shifted to slightly higher 2θ values. The shifts are in the order of $0.1\text{--}0.2^\circ$ and are listed in Table S1 (ESI). A Williamson-Hall plot is constructed from the XRD data of the deposits generated at 21 °C and 120 °C and shown in Fig. S2 (ESI) and discussed in the ESI.

These results indicate that InSb can indeed be electrodeposited at 120 °C. Yet, the InSb films show cracks, and contain a small quantity of pure indium. In addition, there is no evidence of increased crystallinity. Elevated temperature electrodeposition of InSb from a mixed electrolyte did not result in films of superior quality. However, the higher obtained cathodic current densities resulted in a faster deposition rate, which can be regarded as an advantage.

As previously indicated, small mismatch buffers are often used for the vacuum deposition of InSb. To test if the morphology would differ from that seen on platinum, electrodeposition of InSb was carried out on n-type InSb at 120 °C. Since the deposited material's characteristics are identical to those of the substrate, it may be possible to generate deposits without cracks. Due to its small bandgap and the elevated working temperature, n-type InSb could be used as a substrate for electrodeposition as electron transfer is readily possible. Naturally, electrodeposition of InSb on n-type InSb has no real applications. This experiment was only performed to investigate whether changes in morphology would be observed as opposed to the deposited films on the platinum substrates. Electrodeposition was performed under analogous conditions as before, using the 5:1 electrolyte composed of 0.1 M of $\text{In}(\text{CH}_3\text{SO}_3)_3$ and 0.02 M of $\text{Sb}(\text{NO}_3)_3$ in DMSO, and a cathodic overpotential of -1.6 V vs. Ag^+/Ag was applied for 1 h. at 120 °C. In Fig. 7a–c, the SEM images, EDX spectrum and XRD diffractogram are shown, respectively. The EDX spectrum shows peaks for indium and antimony with relative intensities similar to the spectra shown in Figs. 5 and 6. The In/Sb ratio equals 52/48 atomic %. The SEM images show a smooth deposited layer, with a very fine morphology. Furthermore, the layer is free of cracks. This is explained by the identical thermal expansion between the substrate and the deposited InSb as well as the lack of a lattice mismatch. In Fig. 7c, the diffraction peaks of the deposit are shown in black, and that of the neat substrate in red. Given the presence of several diffraction peaks for different orientations, it is obvious that the electrodeposited InSb layer is polycrystalline and not epitaxial.

Fig. 7 **a** SEM images at various magnifications, **b** EDX spectrum, and **c** XRD diffractogram of as-deposited InSb generated by applying -1.6 V vs. Ag^+/Ag for 1 h. on n-type InSb at 120 °C from an electrolyte composed of 0.1 M of $\text{In}(\text{CH}_3\text{SO}_3)_3$ and 0.02 M of $\text{Sb}(\text{NO}_3)_3$ in DMSO. The applied acceleration voltage for EDX and SEM was 10 keV. The XRD peak of the monocrystalline InSb substrate is shown in red



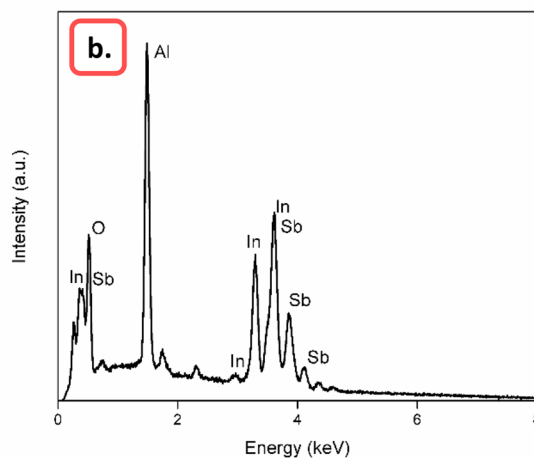
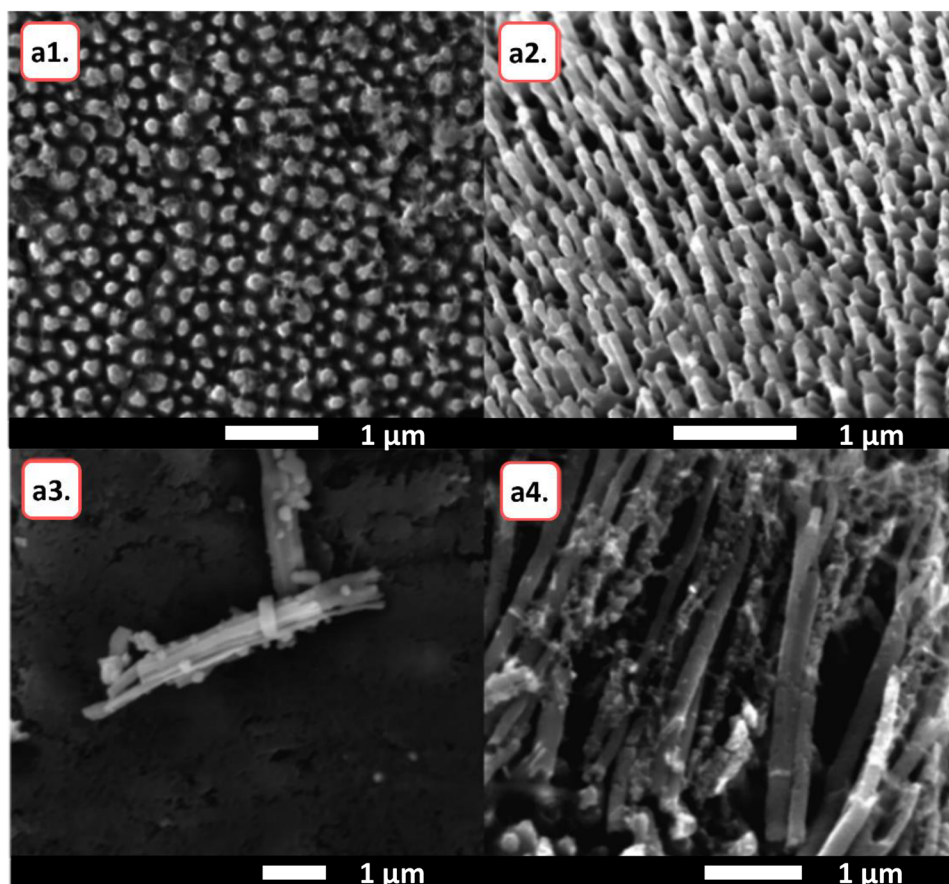
The deposited InSb shows no preference for the (400) orientation of the n-type InSb substrate, as the overlapping peak at 57° is very small as opposed to the other peaks. This is due to the fast nucleation and growth happening during electrodeposition at -1.6 V vs. Ag^+/Ag . Formation of deposits occurs at such a high rate that the orientation of the substrate cannot be followed. To achieve epitaxial deposition, working with very diluted solutions is required if a constant overpotential is applied.

Electrodeposition of InSb nanowires

It was also investigated whether InSb nanowires could be electrodeposited using AAO substrates. It was calculated

that a cathodic charge of -0.48 C was required to completely fill the nanopores (2 μm in height, 0.12 μm in diameter) in an area of 1 cm². Also here, the electrolyte composed of 0.1 M of $\text{In}(\text{CH}_3\text{SO}_3)_3$ and 0.02 M of $\text{Sb}(\text{NO}_3)_3$ in DMSO was used. A potential of -1.6 V vs. Ag^+/Ag was applied for approximately 1.5 h., until the desired charge of -0.48 C was reached. Two samples were generated; for one, the AAO layer was partly etched away whereas for the other, it was fully etched away. The samples were investigated using SEM and EDX. The resulting spectrum and images are shown in Fig. 8. Top view and side view SEM images in Fig. 8a1 and a2 show InSb nanowires sticking out above the partly etched away AAO. The SEM images in Fig. 8a3 and a4 show the released

Fig. 8 **a1, a2** SEM images of InSb wires in a partly etched away AAO matrix, **a3, a4** SEM images of fully released InSb wires, and **b** EDX spectrum of InSb wires. The applied acceleration voltage for EDX and SEM was 10 keV



InSb nanowires. The rough matter surrounding the wires is attributed to undissolved alumina. Removal of undissolved alumina proved to be challenging. Other ways of releasing the nanowires (for instance in acidic solutions) will be explored as part of the planned future work. The EDX spectrum (Fig. 8b) shows peaks for indium, antimony and aluminum and oxygen. The former two can be ascribed to the formation of InSb nanowires, whereas the latter two are due to the partly etched AAO.

Bandgap determination

Lastly, the bandgap E_g of the deposited InSb films at RT on platinum and n-type InSb was determined using a Tauc plot constructed from FT-IR spectra [57, 58]. Tauc plot is based on the following equation:

$$(\alpha h\nu)^n = A^*(h\nu - E_g) \quad (3)$$

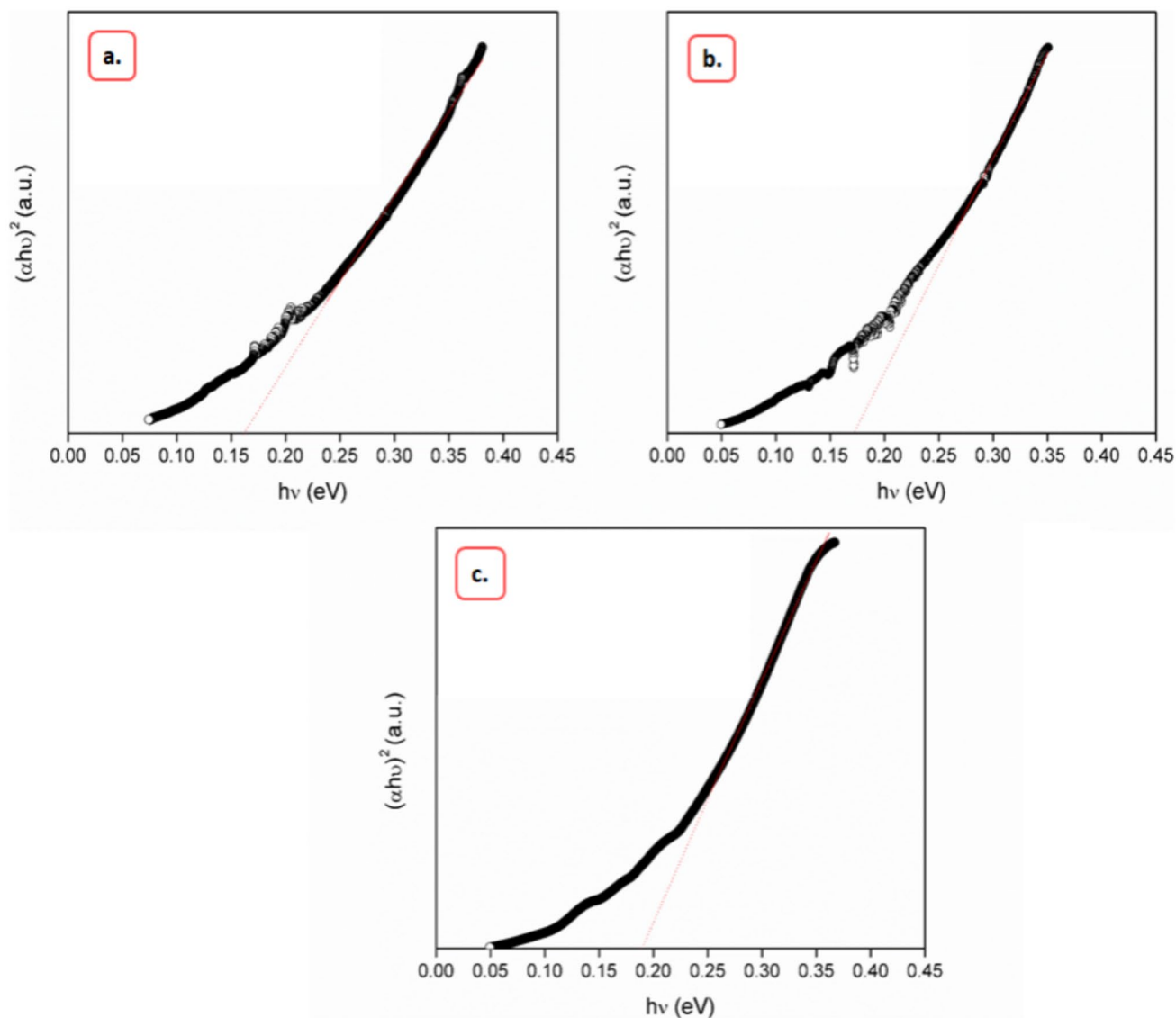


Fig. 9 Modified Tauc plots of InSb films on platinum electrodeposited at **a** 21 °C, **b** 120 °C, and **c** from an InSb film on n-type InSb electrodeposited at 120 °C

where α is the absorption coefficient (m^{-1}), h is Planck's constant ($6.6265 \times 10^{-34} \text{ J} \cdot \text{Hz}^{-1}$), ν is the photon frequency (Hz), and A^* is the slope of the Tauc plot in the linear region. For allowed indirect transitions, $n = 2$. Transparent disks were prepared from the electrodeposited InSb films, for which FT-IR spectra were recorded between 400 cm^{-1} and 4000 cm^{-1} . These spectra are shown in Fig. S3 (ESI) The spectroscopic data were used to calculate the absorption coefficient α and photon energy $h\nu$. α was determined via:

$$\alpha = \ln(10) A L^{-1} \quad (4)$$

where $A = -\log_{10}(T)$, with A the absorbance, L the thickness of the sample and T the transmittance. The $(\alpha h\nu)^2$

versus $h\nu$ plot was subsequently constructed. The resulting curves are shown in Fig. 9. Figure 9a and b represent those attained from the deposits on platinum at 21 °C and 120 °C, respectively, whereas Fig. 9c represents that of the deposit on n-type InSb at 120 °C. For all curves, a good linear fit was obtained, indicating direct transition. From the intercept with the x -axis, E_g equals $0.159 \pm 0.002 \text{ eV}$ for the deposit on platinum at 21 °C, $0.168 \pm 0.002 \text{ eV}$ for the deposit on platinum at 120 °C and $0.186 \pm 0.001 \text{ eV}$ for the deposit on n-type InSb at 120 °C. The linear fit and the corresponding values for the three Tauc plots are shown in Figs. S4, S5 and S6 (ESI), respectively. The obtained bandgap values vary slightly from the reported bandgap of InSb (0.17 eV

at 26.8 °C). However, we want to emphasize that bandgap determination by means of a Tauc plot is crude, as the fit of the straight line depends on the number of points, the way the graph is scaled, and if Urbach tailing is considered [59, 60]. Moreover, the Tauc's method evaluates the bandgap of amorphous (or glassy) materials (in which localization of energy states can be assumed) but has been routinely (and incorrectly) applied to study crystalline and/or highly-doped semiconductors. More suitable methods exist to determine the bandgap of the crystalline semiconductors based on photoluminescence or diffuse-reflectance measurements [61]. These methods will be used in the future to confirm the bandgap of the deposited InSb films and nanowires.

Conclusions

In this work, the electrodeposition of InSb films and nanowires was demonstrated from a non-aqueous DMSO-based electrolyte. $\text{In}(\text{CH}_3\text{SO}_3)_3$ and $\text{Sb}(\text{NO}_3)_3$ were used as precursors, as they enabled pure indium and antimony electrodeposition. Despite its use in several other InSb electrodeposition narratives, it was shown here that SbCl_3 is unsuitable as antimony precursor, as it leads to electrodeposition of metastable “*explosive antimony*”. Mixed electrolytes were prepared with a 5:1 In/Sb ratio, and films and nanowires were electrodeposited at an overpotential of -1.6 V vs. Ag^+/Ag . SEM, EDX and XRD analysis indicated that good quality, polycrystalline InSb films were attained on platinum at 21 °C, whereas cracked, polycrystalline films were attained on platinum at 120 °C. The bandgap of these films was determined using modified Tauc plots and equaled 0.159 ± 0.002 eV at 21 °C and 0.168 ± 0.002 eV at 120 °C. Crack-free polycrystalline films with very fine morphology were attained on n-type InSb at 120 °C. The bandgap of this film was 0.186 ± 0.001 eV. SEM and EDX analysis also revealed that InSb nanowires could be electrodeposited using AAO substrates as template.

Supplementary information The online version contains supplementary material available at <https://doi.org/10.1007/s10008-024-05947-x>.

Acknowledgements The authors thank Phillip Dale for sharing his expertise regarding Tauc's plots. The authors also thank Clement Merckling for providing an n-type InSb wafer piece.

Funding WM thanks the Research Foundation Flanders (FWO) for supporting the research by the PhD grant (1SB8319N).

References

- Afzaal M, O'Brien P (2006) Recent developments in II-VI and III-VI semiconductors and their applications in solar cells. *J Mater Chem* 16:1597–1602
- Li J, Wang D, LaPierre RR (2011) *Advances in III-V semiconductor nanowires and nanodevices*. Bentham Science Publishers
- Adachi S (2009) *Properties of semiconductor alloys: group-IV, III-V and II-VI semiconductors*. John Wiley & Sons
- Adachi S (1992) *Physical properties of III-V semiconductor compounds*. John Wiley & Sons
- Kane EO (1957) Band structure of indium antimonide. *J Phys Chem Solids* 1:249–261
- Hulme KF, Mullin JB (1962) Indium antimonide—a review of its preparation, properties and device applications. *Solid State Electron* 5:211–IN10
- Tanenbaum M, Briggs HB (1953) Optical properties of indium antimonide. *Phys Rev* 91:1561
- Shafa M, Akbar S, Gao L et al (2016) Indium antimonide nanowires: synthesis and properties. *Nanoscale Res Lett* 11:1–20
- Sikorski C, Merkt U (1989) Spectroscopy of electronic states in InSb quantum dots. *Phys Rev Lett* 62:2164
- Smith SJ, Nash GR, Fearn M et al (2006) Photoluminescence from single InSb quantum wells. *Appl Phys Lett* 88:81909
- Van Welzenis RG f, Ridley BK (1984) On the properties of InSb quantum wells. *Solid State Electron* 27:113–120
- Liu W, Chang AY, Schaller RD, Talapin DV (2012) Colloidal insb nanocrystals. *J Am Chem Soc* 134:20258–20261
- Liu WK, Yuen WT, Stradling RA (1995) Preparation of InSb substrates for molecular beam epitaxy. *J Vac Sci Technol B Microelectron Nanometer Struct Process Meas Phenom* 13:1539–1545
- Caroff P, Wagner JB, Dick KA et al (2008) High-quality InAs/InSb nanowire heterostructures grown by metal–organic vapor-phase epitaxy. *Small* 4:878–882
- Ercolani D, Rossi F, Li A et al (2009) InAs/InSb nanowire heterostructures grown by chemical beam epitaxy. *Nanotechnology* 20:505605
- Caroff P, Messing ME, Borg BM et al (2009) InSb heterostructure nanowires: MOVPE growth under extreme lattice mismatch. *Nanotechnology* 20:495606
- Koguchi N, Takahashi S, Chikyow T (1991) New MBE growth method for InSb quantum well boxes. *J Cryst Growth* 111:688–692
- Mahan JE (2000) Physical vapor deposition of thin films
- Fulop GF, Taylor RM (1985) Electrodeposition of semiconductors. *Annu Rev Mater Sci* 15:197–210
- Ruythooren W, Attenborough K, Beerten S et al (2000) Electrodeposition for the synthesis of microsystems. *J Micromech Microeng* 10:101
- Dharmadasa IM, Haigh J (2005) Strengths and advantages of electrodeposition as a semiconductor growth technique for applications in macroelectronic devices. *J Electrochem Soc* 153:G47
- Pandey RK, Sahu SN, Chandra S (2017) *Handbook of semiconductor electrodeposition*. CRC Press
- Hnida KE, Bäßler S, Mech J et al (2016) Electrochemically deposited nanocrystalline InSb thin films and their electrical properties. *J Mater Chem C Mater* 4:1345–1350
- Zhang X, Hao Y, Meng G, Zhang L (2005) Fabrication of highly ordered InSb nanowire arrays by electrodeposition in porous anodic alumina membranes. *J Electrochem Soc* 152:C664
- Das SR, Akatay C, Mohammad A et al (2014) Electrodeposition of InSb branched nanowires: controlled growth with structurally tailored properties. *J Appl Phys* 116:83506
- Hunze A, Granville S, Greenbank W (2016) Magnetoresistance of electrochemically produced InSb. *Mater Res Innovations* 20:518–523
- Mengoli G, Musiani MM, Paolucci F (1992) Synthesis of InAs and InAs_{1-x}Sb_x from electrodeposited layers of indium, arsenic and As Sb alloy. *J Electroanal Chem* 332:199–211
- Singh J, Poolla R (2018) Effect of complexing agents on properties of electrodeposited InSb thin films. *J Electron Mater* 47:6848–6861

29. Hnida K, Mech J, Sulka GD (2013) Template-assisted electrodeposition of indium–antimony nanowires—comparison of electrochemical methods. *Appl Surf Sci* 287:252–256
30. Khan MI, Wang X, Jing X et al (2009) Study of a single InSb nanowire fabricated via DC electrodeposition in porous templates. *J Nanosci Nanotechnol* 9:2639–2644
31. Fulop T, Bekele C, Landau U et al (2004) Electrodeposition of polycrystalline InSb from aqueous electrolytes. *Thin Solid Films* 449:1–5
32. Das SR, Delker CJ, Zakharov D et al (2011) Room temperature device performance of electrodeposited InSb nanowire field effect transistors. *Appl Phys Lett* 98:243504
33. Hnida KE, Marzec M, Wlazlak E et al (2019) Influence of pulse frequency on physicochemical properties of InSb films obtained via electrodeposition. *Electrochim Acta* 304:396–404
34. Rajska D, Brzózka A, Hnida-Gut KE, Sulka GD (2021) Investigation of electrodeposition kinetics of In, Sb, and Zn for advanced designing of InSb and ZnSb thin films. *J Electroanal Chem* 882:114967
35. Singh AP, Roccapiore K, Algarni Z et al (2019) Structure and electronic properties of InSb nanowires grown in flexible polycarbonate membranes. *Nanomaterials* 9:1260
36. Fahrenkrug E, Rafson J, Lancaster M, Maldonado S (2017) Concerted electrodeposition and alloying of antimony on indium electrodes for selective formation of crystalline indium antimonide. *Langmuir* 33:9280–9287
37. Kozlov VM, Agrigento V, Bontempi D et al (1997) Intermetallic compound formed by electrodeposition of indium on antimony. *J Alloys Compd* 259:234–240
38. Yang M-H, Yang M-C, Sun I-W (2003) Electrodeposition of indium antimonide from the water-stable 1-ethyl-3-methylimidazolium chloride/tetrafluoroborate ionic liquid. *J Electrochem Soc* 150:C544
39. Hsieh Y, Chen Y, Sun I (2016) Electrodeposition of stoichiometric indium antimonide from room-temperature ionic liquid 1-butyl-1-methylpyrrolidinium dicyanamide. *ChemElectroChem* 3:638–643
40. Carpenter MK, Verbrugge MW (1994) Electrochemical codeposition of indium and antimony from a chloroindate molten salt. *J Mater Res* 9:2584–2591
41. Monnens W, Deferm C, Binnemans K, Fransaer J (2020) Indium electrodeposition from indium (iii) methanesulfonate in DMSO. *Phys Chem Chem Phys* 22:24526–24534
42. Schoch EP, Brown DJ, Phipps TE (1916) An electro-analytical method for the determination and separation of the metals of the copper-tin group. *J Am Chem Soc* 38:1660–1681
43. Wu M, Binnemans K, Fransaer J (2014) Electrodeposition of antimony from chloride-free ethylene glycol solutions and fabrication of thermoelectric Bi₂Te₃/(Bi_{1-x}Sb_x)₂Te₃ multilayers using pulsed potential electrodeposition. *Electrochim Acta* 147:451–459
44. Sadana YN, Singh JP, Kumar R (1985) Electrodeposition of antimony and antimony alloys—a review. *Surf Technol* 24:319–353
45. Hashimoto H, Nishimura T, Umetsu Y (2003) Hydrolysis of antimony (III)-hydrochloric acid solution at 25 °C. *Mater Trans* 44:1624–1629
46. Liu J, Zhang Y, Guo C (2013) Thermodynamic assessment of the Pt-Sb system
47. Kushvaha SS, Yan Z, Xiao W, Wang XS (2006) Surface morphology of crystalline antimony islands on graphite at room temperature. *J Phys Condens Matter* 18:3425
48. Kozlov VM, Agrigento V, Mussati G, Bicelli LP (1999) Influence of the structure of the electrodeposited antimony substrate on indium diffusion. *J Alloys Compd* 288:255–261
49. Yang M-H, Sun I-W (2003) Electrodeposition of antimony in a water-stable 1-ethyl-3-methylimidazolium chloride tetrafluoroborate room temperature ionic liquid. *J Appl Electrochem* 33:1077–1084
50. Lobaccaro P, Raygani A, Oriani A et al (2014) Electrodeposition of high-purity indium thin films and its application to indium phosphide solar cells. *J Electrochem Soc* 161:D794
51. Neumann AN, Schneble OD, Warren EL (2022) Communication—electrodeposition of indium directly on silicon. *J Electrochem Soc* 169:012503
52. Monnens W, Deferm C, Sniekers J et al (2019) Electrodeposition of indium from non-aqueous electrolytes. *Chem Commun* 55:4789–4792
53. Sharma RC, Ngai TL, Chang YA (1989) The In-Sb (indium-antimony) system. *Bull Alloy Phase Diagrams* 10:657–664
54. Anderson TJ, Donaghey LF (1984) Solid-state electrochemical study of In-Sb liquid alloys. *J Electrochem Soc* 131:3006
55. Boley BA, Weiner JH (2012) Theory of thermal stresses. Courier Corporation
56. Mori M, Akae N, Uotani K et al (2003) Heteroepitaxial growth of InSb films on a Si (0 0 1) substrate via AlSb buffer layer. *Appl Surf Sci* 216:569–574
57. Tauc J (1968) Optical properties and electronic structure of amorphous Ge and Si. *Mater Res Bull* 3:37–46
58. Vezbicke BD, Patel S, Davis BE, Birnie DP III (2015) Evaluation of the Tauc method for optical absorption edge determination: ZnO thin films as a model system. *Phys Status Solidi B* 252:1700–1710
59. Zanatta AR (2019) Revisiting the optical bandgap of semiconductors and the proposal of a unified methodology to its determination. *Sci Rep* 9:1–12
60. Dolgonos A, Mason TO, Poepfelmeier KR (2016) Direct optical band gap measurement in polycrystalline semiconductors: a critical look at the Tauc method. *J Solid State Chem* 240:43–48
61. Gozu S-I (2022) Photoluminescence of an InSb layer on a germanium substrate. *Semicond Sci Technol* 37:65002

Publisher's note Springer Nature remains neutral with regard to jurisdictional claims in published maps and institutional affiliations.

Springer Nature or its licensor (e.g. a society or other partner) holds exclusive rights to this article under a publishing agreement with the author(s) or other rightsholder(s); author self-archiving of the accepted manuscript version of this article is solely governed by the terms of such publishing agreement and applicable law.